

Theory of exciton dephasing in semiconductor quantum dots

T. Takagahara

NTT Basic Research Laboratories, 3-1 Morinosato Wakamiya, Atsugi-shi, 243-0198, Japan

(Received 11 January 1999)

We formulate a theory of exciton dephasing in semiconductor quantum dots extending the Huang-Rhys theory of F centers to include the mixing among the exciton state manifold through the exciton-acoustic-phonon interaction and we identify the mechanisms of pure dephasing. We can reproduce quantitatively the magnitude as well as the temperature dependence of the exciton dephasing rate observed in GaAs quantum dotlike islands. In this system it turns out that both the diagonal and off-diagonal exciton-phonon interactions are contributing to the exciton pure dephasing on the same order of magnitude. Examining the previous data of the exciton dephasing rate in GaAs islands, CuCl and CdSe nanocrystals, we point out the correlation between the temperature dependence of the dephasing rate and the strength of the quantum confinement and we explain the gross features of the temperature dependence in various materials quantum dots. Furthermore, we discuss likely mechanisms of the exciton population decay. [S0163-1829(99)02728-9]

I. INTRODUCTION

A resonant optical excitation creates an excited-state population and also induces an optical polarization. The dynamics of this optical excitation is characterized by the relaxation of the population as well as the decay of the induced optical polarization. In lower-dimensional semiconductors, electronic confinement leads to qualitative changes in the population relaxation, including spontaneous emission and exciton-phonon scattering, as shown in extensive recent studies.¹ These population relaxation processes are expected to contribute to dephasing with a dephasing rate given by half the population decay rate. Pure dephasing processes that do not involve population or energy relaxation of excitons can also contribute to dephasing. Pure dephasing, which is a well-established concept for atomic systems, remains yet to be investigated in lower-dimensional semiconductors due to a lack of direct comparison between dephasing and population relaxation and between theory and experiment. Studies of pure dephasing processes in lower-dimensional semiconductors will renew and deepen our understanding of the dephasing of collective excitations in solids, although several seminal studies were done on the exciton dephasing in quantum well (QW) structures.²⁻⁶

Narrow GaAs QW's grown by molecular-beam epitaxy (MBE) and with growth interruptions have provided a model system for investigating dephasing processes in lower-dimensional semiconductors. In these narrow QW's, fluctuations at the interface between GaAs and $\text{Al}_{1-x}\text{Ga}_x\text{As}$ lead to the localization of excitons at monolayer-high islands. These localized states can be regarded effectively as weakly confined quantum dot (QD) like states. One dimension of the confinement is defined by the width of the QW, while the other two lateral dimensions are defined by the effective size of the islands. To avoid inhomogeneous broadening due to well-width and island-size fluctuations, earlier studies have used photoluminescence (PL) and PL excitation with high spatial resolution to probe excitons in individual islands.⁷⁻⁹

As a result, a very narrow linewidth of about several tens of μeV was observed. Without additional information on population relaxation, it was suggested that at very low temperatures dephasing of excitons in these structures is due to radiative recombination, while at elevated temperatures dephasing is mainly caused by the thermal activation of excitons to higher excited states.⁹ However, this interpretation is not complete since both of the suggested processes belong to the longitudinal decay processes and the dephasing rate is in general composed of half the longitudinal decay rate and the pure dephasing rate. In order to examine the presence of a pure dephasing in this system, we carried out nonlinear optical measurements of the exciton dephasing in GaAs QD-like islands based on the three-pulse stimulated photon-echo method.¹⁰ This method enables the simultaneous measurement of the dephasing rate and the population decay rate. At very low temperatures the observed dephasing rate Γ_{\perp} is very close to half the population decay rate $\Gamma_{\parallel}/2$, suggesting that dephasing is caused mainly by the population decay. With increasing temperature the dephasing rate increases much faster than the population decay rate. At elevated temperatures (>30 K), dephasing rates become much greater than $\Gamma_{\parallel}/2$, indicating a dominant contribution of pure dephasing. Thus our measurements revealed convincingly the presence of pure dephasing process that dominates excitonic dephasing at elevated temperatures.

The observed strong increase of the pure dephasing rate above 30 K suggests that interactions between excitons and low-energy acoustic phonons play an essential role in the pure dephasing process. In this paper we present a theoretical model that takes into account the interaction between excitons and acoustic phonons and can explain satisfactorily the magnitude as well as the temperature dependence of the dephasing rate. Our model generalizes the Huang-Rhys theory of F centers¹¹⁻¹³ by including mixing among the ground and excited exciton states through exciton-phonon interactions and as a result enables us to identify the elementary processes of exciton pure dephasing.

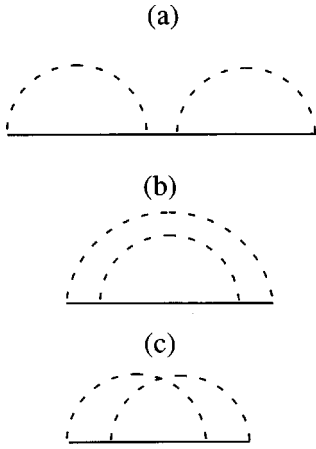


FIG. 1. Possible diagrams of the fourth-order term in Eq. (2.6). A solid (dashed) line denotes the exciton (phonon) propagator.

A comparison of the observed temperature dependence of the exciton dephasing rate in GaAs QD-like islands with the previously reported temperature dependence for CdSe (Ref. 14) and CuCl (Ref. 15) nanocrystals suggests qualitative differences dependent on the strength of quantum confinement. In the strong confinement regime as in CdSe nanocrystals, linear temperature dependence prevails up to high temperatures (~ 200 K). On the other hand, in the weak confinement regime, as in GaAs islands and CuCl nanocrystals, the linear temperature dependence is dominated by the nonlinear temperature dependence with increasing temperature. It is very important to clarify the underlying physics of these differences.

In Sec. II a theory of exciton dephasing is formulated quite generally in terms of Green functions. The interaction Hamiltonians between excitons and acoustic phonons are given explicitly in Sec. III. A quantum disk model to simulate a QD-like island in QW's is described in detail and typical exciton level structures are exhibited in Sec. IV. In Sec. V the calculated exciton dephasing rates and their temperature dependence are discussed in comparison with our previously published experimental results¹⁰ and the presence of exciton pure dephasing is confirmed. In Sec. VI the elementary processes of the exciton pure dephasing are identified. Pure dephasing arises from virtual processes and there are two kinds of such processes. The physical meaning of these two processes is discussed. In Sec. VII the likely mechanisms of the population decay of excitons are identified in comparison with experimental data. In Sec. VIII the underlying physics will be clarified concerning the relationship between the temperature dependence of the exciton dephasing rate and the strength of the quantum confinement. Finally, Sec. IX is devoted to the summary and discussion.

II. GREEN-FUNCTION FORMALISM OF THE EXCITON DEPHASING RATE

As discussed in the Introduction, the strong increase of the exciton dephasing rate above 30 K suggests the important role of the low-energy acoustic phonons in determining the dephasing rate. The exciton dephasing rate can be estimated most directly from the half-width at half maximum

(HWHM) of the absorption spectrum, which can be calculated from the Fermi golden rule as

$$I(\hbar\omega) = \frac{2\pi}{\hbar} A_{\text{av}} \sum_f | \langle f | V_R | g \rangle |^2 \delta(\hbar\omega + E_g - E_f), \quad (2.1)$$

where V_R is the electromagnetic interaction, $|f\rangle$ and $|g\rangle$ denote the final exciton state and the initial ground state, respectively, including the phonon degrees of freedom, and A_{av} means the average over the thermal equilibrium state of phonons. This expression can be rewritten as

$$I(\hbar\omega) \propto \text{Re} \left\{ \int_0^\infty dt e^{-i\omega t} A_{\text{av}} \langle g | V_R \exp \left[\frac{i}{\hbar} H_e t \right] V_R \exp \left[-\frac{i}{\hbar} H_g t \right] | g \rangle \right\}, \quad (2.2)$$

where H_e and H_g are the Hamiltonians of the excited state and the ground state, respectively. This can be confirmed by inserting a closure relation between two V_R 's. Equation (2.2) is a Fourier-Laplace transform of a correlation function. In order to proceed further, the Hamiltonians will be specified as

$$H_g = \sum_\alpha \hbar \omega_\alpha b_\alpha^\dagger b_\alpha, \quad (2.3)$$

$$H_e = \sum_i E_i |i\rangle \langle i| + \sum_\alpha \hbar \omega_\alpha b_\alpha^\dagger b_\alpha + \sum_\alpha M_\alpha (b_\alpha + b_\alpha^\dagger), \quad (2.4)$$

where the index α denotes the acoustic-phonon mode, E_i the energy of the exciton states, and M_α is the exciton-phonon coupling matrix within the exciton state manifold. This is a generalization of the Huang-Rhys model of F centers¹¹ to include mixing among the exciton state manifold which is reflected in the matrix form of M_α . In the following, we take into account only the exciton-phonon coupling which is linear with respect to the phonon coordinates. Even within this range, however, the well-known deformation potential coupling and the piezoelectric coupling are included. Thus our Hamiltonian is sufficiently general. We note that in the elementary processes of the exciton-phonon interaction the crystal momentum conservation needs to be satisfied in directions where the translational invariance holds. The dephasing process becomes prominent in systems with three-dimensional (3D) electronic confinement because the 3D confinement relaxes the crystal momentum conservation and also suppresses exciton population relaxation^{16,17} due to the exciton-phonon interactions.

Hereafter the three terms of H_e in Eq. (2.4) will be denoted, respectively, as

$$H_e = H_e^0 + H_g + V. \quad (2.5)$$

Then the Laplace transform of $\exp[(i/\hbar)H_e t]$ can be expanded as

$$\int_0^\infty dt e^{-st} \exp[(i/\hbar)H_e t] = \frac{1}{s - \frac{i}{\hbar}H_e} = \frac{1}{s - \frac{i}{\hbar}(H_e^0 + H_g)} + \frac{i}{\hbar} \frac{1}{s - \frac{i}{\hbar}(H_e^0 + H_g)} V \frac{1}{s - \frac{i}{\hbar}(H_e^0 + H_g)} \\ + \left(\frac{i}{\hbar}\right)^2 \frac{1}{s - \frac{i}{\hbar}(H_e^0 + H_g)} V \frac{1}{s - \frac{i}{\hbar}(H_e^0 + H_g)} V \frac{1}{s - \frac{i}{\hbar}(H_e^0 + H_g)} + \dots \quad (2.6)$$

For example, the third term on the right-hand side of Eq. (2.6) can be expressed in the convolution form as

$$\left(\frac{i}{\hbar}\right)^2 \int_0^t dt_1 \int_0^{t_1} dt_2 e^{(i/\hbar)(H_e^0 + H_g)(t-t_1)} V e^{(i/\hbar)(H_e^0 + H_g)(t_1-t_2)} V e^{(i/\hbar)(H_e^0 + H_g)t_2}. \quad (2.7)$$

Substituting this term for $\exp[(i/\hbar)H_e t]$ in Eq. (2.2) and noting the commutability between H_e^0 and H_g and between M_α and H_g , we have

$$\langle g | V_R \exp\left[\frac{i}{\hbar}H_e t\right] V_R \exp\left[-\frac{i}{\hbar}H_g t\right] |g\rangle \rightarrow \left(\frac{i}{\hbar}\right)^2 \int_0^t dt_1 \int_0^{t_1} dt_2 \sum_{\alpha,\beta} \langle g | V_R \exp\left[\frac{i}{\hbar}H_e^0(t-t_1)\right] M_\alpha \exp\left[\frac{i}{\hbar}H_e^0(t_1-t_2)\right] \\ \times M_\beta \exp\left[\frac{i}{\hbar}H_e^0 t_2\right] V_R |g\rangle \langle 0 | \exp\left[\frac{i}{\hbar}H_g(t-t_1)\right] (b_\alpha + b_\alpha^\dagger) \exp\left[\frac{i}{\hbar}H_g(t_1-t_2)\right] \\ \times (b_\beta + b_\beta^\dagger) \exp\left[\frac{i}{\hbar}H_g t_2\right] \exp\left[-\frac{i}{\hbar}H_g t\right] |0\rangle, \quad (2.8)$$

where $|0\rangle$ denotes symbolically the thermal equilibrium state of phonons. The phonon part of Eq. (2.8) can be written as

$$\langle 0 | \exp\left[\frac{i}{\hbar}H_g(t-t_1)\right] (b_\alpha + b_\alpha^\dagger) \exp\left[\frac{i}{\hbar}H_g(t_1-t_2)\right] (b_\beta + b_\beta^\dagger) \exp\left[\frac{i}{\hbar}H_g t_2\right] \exp\left[-\frac{i}{\hbar}H_g t\right] |0\rangle \\ = \text{Tr } \rho_0 \exp\left[-\frac{i}{\hbar}H_g t_1\right] (b_\alpha + b_\alpha^\dagger) \exp\left[\frac{i}{\hbar}H_g(t_1-t_2)\right] (b_\beta + b_\beta^\dagger) \exp\left[\frac{i}{\hbar}H_g t_2\right] \\ = \text{Tr } \rho_0 (b_\alpha(-t_1) + b_\alpha^\dagger(-t_1)) (b_\beta(-t_2) + b_\beta^\dagger(-t_2)) \\ = \delta_{\alpha\beta} [N_\alpha e^{-i\omega_\alpha(t_1-t_2)} + (1+N_\alpha) e^{i\omega_\alpha(t_1-t_2)}] \quad (2.9)$$

with

$$\rho_0 = e^{-\beta H_g} / \text{Tr } e^{-\beta H_g},$$

$$b_\alpha(t) = \exp\left[\frac{i}{\hbar}H_g t\right] b_\alpha \exp\left[-\frac{i}{\hbar}H_g t\right] = e^{-i\omega_\alpha t} b_\alpha,$$

and

$$N_\alpha = 1 / [\exp(\beta \hbar \omega_\alpha) - 1] \quad \text{with} \quad \beta = 1/(k_B T).$$

Then again making a Laplace transform, we have

$$\left(\frac{i}{\hbar}\right)^2 \langle g | V_R \frac{1}{s - \frac{i}{\hbar}H_e^0} \sum_\alpha M_\alpha \left\{ \frac{N_\alpha}{s - \frac{i}{\hbar}H_e^0 + i\omega_\alpha} + \frac{1+N_\alpha}{s - \frac{i}{\hbar}H_e^0 - i\omega_\alpha} \right\} M_\alpha \frac{1}{s - \frac{i}{\hbar}H_e^0} V_R |g\rangle = \langle g | V_R \frac{1}{s - \frac{i}{\hbar}H_e^0} \Sigma_0^{(2)}(s) \frac{1}{s - \frac{i}{\hbar}H_e^0} V_R |g\rangle \quad (2.10)$$

with

$$\Sigma_0^{(2)}(s) = \left(\frac{i}{\hbar}\right)^2 \sum_\alpha M_\alpha \left\{ \frac{N_\alpha}{s - \frac{i}{\hbar}H_e^0 + i\omega_\alpha} + \frac{1+N_\alpha}{s - \frac{i}{\hbar}H_e^0 - i\omega_\alpha} \right\} M_\alpha. \quad (2.11)$$

Since the exciton-phonon interaction Hamiltonian V is linear with respect to the phonon coordinates, the terms of odd powers in V in Eq. (2.6) vanish in the final expression. The next nonvanishing term is the fourth-order term in V and this has three contraction diagrams as depicted in Fig. 1. For example, the term corresponding to Fig. 1(c) can be written as

$$\begin{aligned} \Sigma_0^{(4)}(s) = & \left(\frac{i}{\hbar}\right)^4 \sum_{\alpha,\beta} \left\{ M_\alpha \frac{N_\alpha}{s - \frac{i}{\hbar}H_e^0 + i\omega_\alpha} M_\beta \frac{1}{s - \frac{i}{\hbar}H_e^0 + i(\omega_\alpha + \omega_\beta)} M_\alpha \frac{N_\beta}{s - \frac{i}{\hbar}H_e^0 + i\omega_\beta} M_\beta \right. \\ & + M_\alpha \frac{N_\alpha}{s - \frac{i}{\hbar}H_e^0 + i\omega_\alpha} M_\beta \frac{1}{s - \frac{i}{\hbar}H_e^0 + i(\omega_\alpha - \omega_\beta)} M_\alpha \frac{1 + N_\beta}{s - \frac{i}{\hbar}H_e^0 - i\omega_\beta} M_\beta \\ & + M_\alpha \frac{1 + N_\alpha}{s - \frac{i}{\hbar}H_e^0 - i\omega_\alpha} M_\beta \frac{1}{s - \frac{i}{\hbar}H_e^0 - i(\omega_\alpha - \omega_\beta)} M_\alpha \frac{N_\beta}{s - \frac{i}{\hbar}H_e^0 + i\omega_\beta} M_\beta \\ & \left. + M_\alpha \frac{1 + N_\alpha}{s - \frac{i}{\hbar}H_e^0 - i\omega_\alpha} M_\beta \frac{1}{s - \frac{i}{\hbar}H_e^0 - i(\omega_\alpha + \omega_\beta)} M_\alpha \frac{1 + N_\beta}{s - \frac{i}{\hbar}H_e^0 - i\omega_\beta} M_\beta \right\}. \end{aligned} \quad (2.12)$$

On the other hand, the diagrams in Figs. 1(a) and 1(b) can be incorporated into the zeroth-order and second-order terms, respectively, by renormalizing the exciton propagator and the self-energy, as will be shown below.

First of all, we introduce the Green function defined by

$$\begin{aligned} G_0^{(2)}(s) &= \frac{1}{s - \frac{i}{\hbar}H_e^0 - \Sigma_0^{(2)}(s)} \\ &= \frac{1}{s - \frac{i}{\hbar}H_e^0} + \frac{1}{s - \frac{i}{\hbar}H_e^0} \Sigma_0^{(2)}(s) \frac{1}{s - \frac{i}{\hbar}H_e^0} \\ &+ \frac{1}{s - \frac{i}{\hbar}H_e^0} \Sigma_0^{(2)}(s) \frac{1}{s - \frac{i}{\hbar}H_e^0} \Sigma_0^{(2)}(s) \frac{1}{s - \frac{i}{\hbar}H_e^0} \\ &+ \dots, \end{aligned} \quad (2.13)$$

where $\Sigma_0^{(2)}$ is the second-order self-energy and $G_0^{(2)}$ represents the exciton propagator in the phonon field. The dia-

gram in Fig. 1(a) is included in this Green function. Using this propagator, we improve the second-order self-energy as

$$\begin{aligned} \Sigma^{(2)}(s) &= \left(\frac{i}{\hbar}\right)^2 \sum_\alpha M_\alpha [N_\alpha G_0^{(2)}(s + i\omega_\alpha) \\ &+ (1 + N_\alpha) G_0^{(2)}(s - i\omega_\alpha)] M_\alpha, \end{aligned} \quad (2.14)$$

and by incorporating this self-energy into the denominator, we obtain the improved Green function as

$$G^{(2)}(s) = \frac{1}{s - \frac{i}{\hbar}H_e^0 - \Sigma^{(2)}(s)}. \quad (2.15)$$

This Green function incorporates the diagram in Fig. 1(b). Thus only the diagram in Fig. 1(c), namely, an irreducible diagram, should be included in the fourth order.

Now, using the exciton propagator in Eq. (2.15), we calculate the self-energy, including the fourth-order irreducible diagram, namely,

$$\begin{aligned} \Sigma^{(2)}(s) + \Sigma^{(4)}(s) &= \left(\frac{i}{\hbar}\right)^2 \sum_\alpha M_\alpha [N_\alpha G^{(2)}(s + i\omega_\alpha) + (1 + N_\alpha) G^{(2)}(s - i\omega_\alpha)] M_\alpha \\ &+ \left(\frac{i}{\hbar}\right)^4 \sum_{\alpha,\beta} \{ N_\alpha N_\beta M_\alpha G^{(2)}(s + i\omega_\alpha) M_\beta G^{(2)}(s + i(\omega_\alpha + \omega_\beta)) M_\alpha G^{(2)}(s + i\omega_\beta) M_\beta \\ &+ N_\alpha (1 + N_\beta) M_\alpha G^{(2)}(s + i\omega_\alpha) M_\beta G^{(2)}(s + i(\omega_\alpha - \omega_\beta)) M_\alpha G^{(2)}(s - i\omega_\beta) M_\beta \\ &+ (1 + N_\alpha) N_\beta M_\alpha G^{(2)}(s - i\omega_\alpha) M_\beta G^{(2)}(s - i(\omega_\alpha - \omega_\beta)) M_\alpha G^{(2)}(s + i\omega_\beta) M_\beta \\ &+ (1 + N_\alpha) (1 + N_\beta) M_\alpha G^{(2)}(s - i\omega_\alpha) M_\beta G^{(2)}(s - i(\omega_\alpha + \omega_\beta)) M_\alpha G^{(2)}(s - i\omega_\beta) M_\beta \} \end{aligned} \quad (2.16)$$

and incorporating this self-energy into the denominator, we have the improved Green function as

$$G^{(4)}(s) = \frac{1}{s - \frac{i}{\hbar} H_e^0 - \Sigma^{(2)}(s) - \Sigma^{(4)}(s)}. \quad (2.17)$$

We can extend this procedure up to the higher-order iteratively.

As a consequence, we find

$$\begin{aligned} & \int_0^\infty dt e^{-st} A_{\text{av}} \langle g | V_R \exp\left[\frac{i}{\hbar} H_e t\right] V_R \exp\left[-\frac{i}{\hbar} H_g t\right] | g \rangle \\ &= \langle g | V_R \frac{1}{s - \frac{i}{\hbar} H_e^0 - \Sigma(s)} V_R | g \rangle \end{aligned} \quad (2.18)$$

with

$$\Sigma(s) = \Sigma^{(2)}(s) + \Sigma^{(4)}(s) + \Sigma^{(6)}(s) + \dots,$$

where the self-energy parts can be represented by irreducible diagrams as shown in Fig. 2.

The optical-absorption spectrum is calculated from Eq. (2.18) by setting s as

$$s \rightarrow i\omega + \delta,$$

where δ is half of the population decay rate of the exciton state, excluding the contribution from the acoustic-phonon-mediated relaxation, because such contribution is automatically included in the self-energy part $\Sigma(s)$. More concretely, δ should include the radiative decay rate, the trapping rate to some defects, and the rate of exciton migration to neighboring islands. The latter two processes are phonon-mediated but should be included in δ because they are not taken into account in the present Green-function formalism. δ can be estimated from the observed population decay rate subtracting the phonon-assisted population decay rate within an island which can be calculated theoretically as given in Sec. VII.

In order to examine the convergence of the above procedure, we have estimated the Green function up to the sixth order and compared the optical-absorption spectrum and its HWHM by calculating

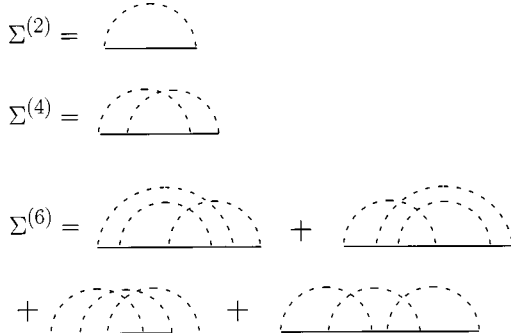


FIG. 2. Irreducible diagrams corresponding to the self-energy terms of the second, fourth, and sixth order with respect to the exciton-phonon interaction.

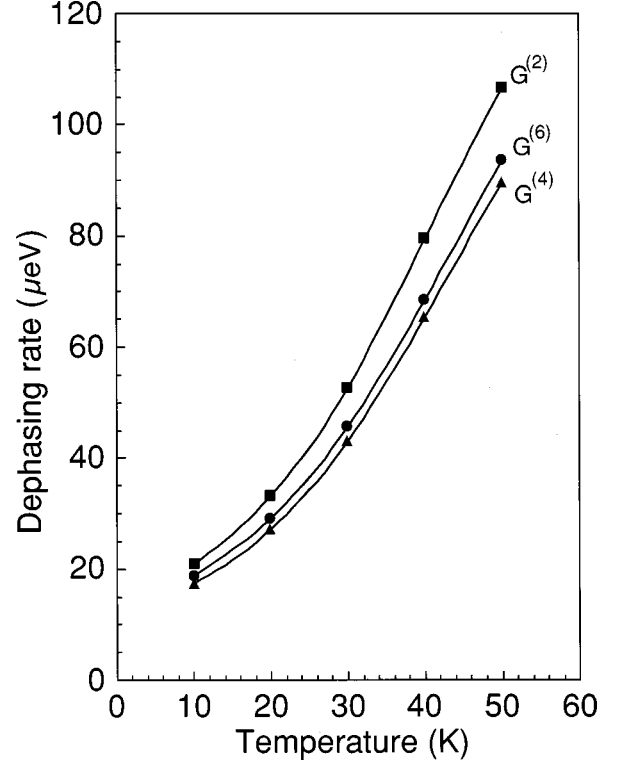


FIG. 3. Temperature dependence of exciton dephasing rates calculated by including the self-energy terms up to the second, fourth, and sixth order denoted as $G^{(2)}$, $G^{(4)}$, and $G^{(6)}$, respectively. The size parameters of the quantum disk are the same as in Fig. 4.

$$I^{(2)}(\omega) = \text{Re}[A_{\text{av}} \langle g | V_R G^{(2)}(s = i\omega + \delta) V_R | g \rangle],$$

$$I^{(4)}(\omega) = \text{Re}[A_{\text{av}} \langle g | V_R G^{(4)}(s = i\omega + \delta) V_R | g \rangle],$$

$$I^{(6)}(\omega) = \text{Re}[A_{\text{av}} \langle g | V_R G^{(6)}(s = i\omega + \delta) V_R | g \rangle]. \quad (2.19)$$

Typical results are shown in Fig. 3. The relevant parameters are explained in Sec. IV. The size parameters of a quantum disk for Fig. 3 are $a = 20$ nm and $b = 15$ nm. It is seen that the percentage difference of the dephasing rates calculated from $G^{(2)}$ and $G^{(4)}$ is about 15–20 %, whereas that calculated from $G^{(4)}$ and $G^{(6)}$ is about several %. Hence we carry out the calculation up to the fourth order and estimate the dephasing rate from the HWHM of $I^{(4)}(\omega)$.

III. EXCITON-PHONON INTERACTIONS

The microscopic details of the interaction Hamiltonian between the exciton and the acoustic phonons will be described. In GaAs/Al_{1-x}Ga_xAs QW's, the elastic properties of both materials are not much different and thus the bulklike acoustic-phonon modes can be assumed as the zeroth-order approximation. Hereafter the phonon modes will be specified by the wave vector \vec{q} . The interaction between electrons and acoustic phonons arises from the deformation potential coupling and the piezoelectric coupling.¹⁸

The dominant interaction term of the deformation potential coupling is given as

$$H_{DF} = \sum_{r,q} \sqrt{\frac{\hbar|q|}{2\rho uV}} (D_c a_{cr}^\dagger a_{cr} + D_v a_{vr}^\dagger a_{vr}) e^{iqr} (b_q + b_{-q}^\dagger), \quad (3.1)$$

where a (a^\dagger) denotes the annihilation (creation) operator of the electron in the conduction (c) or valence (v) band, b (b^\dagger) is the annihilation (creation) operator of the acoustic phonon, D_c (D_v) the deformation potential of the conduction (valence) band, u the sound velocity of the longitudinal-acoustic (LA) mode, V the quantization volume, ρ the mass density, and the vector symbols of \vec{r} and \vec{q} are dropped.

The piezoelectric coupling is given as

$$H_{PZ} = - \sum_{r,q} \frac{8\pi e e_{14}}{\epsilon q^2} \sqrt{\frac{\hbar}{2\rho u|q|V}} (\xi_x q_y q_z + \xi_y q_z q_x + \xi_z q_x q_y) e^{iqr} (a_{cr}^\dagger a_{cr} + a_{vr}^\dagger a_{vr}) (b_q + b_{-q}^\dagger), \quad (3.2)$$

where ϵ (e_{14}) is the dielectric (piezoelectric) constant and $\vec{\xi}$ is the polarization vector of the acoustic-phonon modes. In this case the transverse-acoustic (TA) mode as well as the longitudinal-acoustic (LA) mode contribute to the coupling. The polarization vectors for the LA mode and the two TA modes with a wave vector \vec{q} are given as

$$\begin{aligned} \vec{\xi}(LA) &= (q_x, q_y, q_z) / |\vec{q}|, \\ \vec{\xi}(TA1) &= (q_y, -q_x, 0) / \sqrt{q_x^2 + q_y^2}, \\ \vec{\xi}(TA2) &= (-q_x q_z, -q_y q_z, q_x^2 + q_y^2) / |\vec{q}| \sqrt{q_x^2 + q_y^2}. \end{aligned} \quad (3.3)$$

Then the matrix element of the interaction Hamiltonian between two exciton states given by

$$|X_i\rangle = \sum_{r_e, r_h} F_i(r_e, r_h) a_{cr_e}^\dagger a_{vr_h} |0\rangle \quad (3.4)$$

and

$$|X_f\rangle = \sum_{r_e, r_h} F_f(r_e, r_h) a_{cr_e}^\dagger a_{vr_h} |0\rangle \quad (3.5)$$

is calculated as

$$\begin{aligned} \langle X_f | H_{DF} | X_i \rangle &= \sum_q \sqrt{\frac{\hbar|q|}{2\rho u_{LA}V}} (D_c \langle X_f | e^{iqr_e} | X_i \rangle \\ &\quad - D_v \langle X_f | e^{iqr_h} | X_i \rangle) (\sqrt{N_q} \text{ or } \sqrt{N_q + 1}), \\ \langle X_f | H_{PZ} | X_i \rangle &= - \sum_q \frac{8\pi e e_{14}}{\epsilon q^2} \sqrt{\frac{\hbar}{2\rho u_\sigma |q|V}} \\ &\quad \times (\xi_x q_y q_z + \xi_y q_z q_x + \xi_z q_x q_y) (\langle X_f | e^{iqr_e} | X_i \rangle \\ &\quad - \langle X_f | e^{iqr_h} | X_i \rangle) (\sqrt{N_q} \text{ or } \sqrt{N_q + 1}) \end{aligned} \quad (3.6)$$

with

$$\begin{aligned} \langle X_f | e^{iqr_e(r_h)} | X_i \rangle \\ = \int d^3 r_e \int d^3 r_h F_f^*(r_e, r_h) e^{iqr_e(r_h)} F_i(r_e, r_h), \end{aligned} \quad (3.7)$$

where $\sigma = \text{LA, TA1, and TA2}$ and the factor $\sqrt{N_q}$ ($\sqrt{N_q + 1}$) corresponds to the phonon absorption (emission) process.

The parameter values employed for GaAs are $D_c = -14.6$ eV, $D_v = -4.8$ eV,¹⁹ $u_{LA} = 4.81 \times 10^5$ cm/s, $u_{TA} = 3.34 \times 10^5$ cm/s, $e_{14} = 1.6 \times 10^{-5}$ C/cm², and $\epsilon = 12.56$.²⁰

IV. EXCITONS IN ANISOTROPIC QUANTUM DISK

Now the theoretical formulation has been completed. In a more concrete calculation, we have to specify a model for the QD-like island structures. The extremely narrow linewidth of exciton emission was observed in QW samples.⁷⁻⁹ The lateral fluctuation of the QW thickness gives rise to an islandlike structure. The localized excitons at such structures can be viewed as the zero-dimensional excitons. In these samples, the confinement in the direction of the crystal growth is strong, whereas the confinement in the lateral direction is rather weak. Furthermore, the island structures were found to be elongated along the $[1\bar{1}0]$ direction.⁹ Thus these island structures can be modeled by an anisotropic quantum disk. In order to facilitate the calculation, the lateral confinement potential in the x and y directions is assumed to be Gaussian as

$$\begin{aligned} V_e(r) &= V_e^0 \exp\left[-\left(\frac{x}{a}\right)^2 - \left(\frac{y}{b}\right)^2\right], \\ V_h(r) &= V_h^0 \exp\left[-\left(\frac{x}{a}\right)^2 - \left(\frac{y}{b}\right)^2\right], \end{aligned} \quad (4.1)$$

where the lateral size parameters a and b can be fixed in principle from the measurement of morphology by, e.g., STM, but are left as adjustable parameters. The exciton wave function in such an anisotropic quantum disk can be approximated as

$$\begin{aligned} F(r_e, r_h) &= \sum_{l_e, l_h, m_e, m_h} C(l_e, l_h, m_e, m_h) \\ &\quad \times \left(\frac{x_e}{a}\right)^{l_e} \left(\frac{x_h}{a}\right)^{l_h} \left(\frac{y_e}{b}\right)^{m_e} \left(\frac{y_h}{b}\right)^{m_h} \\ &\quad \times \exp\left[-\frac{1}{2}\left\{\left(\frac{x_e}{a}\right)^2 + \left(\frac{x_h}{a}\right)^2 + \left(\frac{y_e}{b}\right)^2 + \left(\frac{y_h}{b}\right)^2\right\}\right] \\ &\quad - \alpha_x (x_e - x_h)^2 - \alpha_y (y_e - y_h)^2 \Big] \varphi_0(z_e) \varphi_0(z_h) \end{aligned} \quad (4.2)$$

with

$$\varphi_0(z) = \sqrt{\frac{2}{L_z}} \cos\left(\frac{\pi z}{L_z}\right), \quad (4.3)$$

where $C(l_e, l_h, m_e, m_h)$ is the expansion coefficient, L_z is the QW thickness, the factor 1/2 in the exponent is attached to make the probability distribution $|F(r_e, r_h)|^2$ follow the

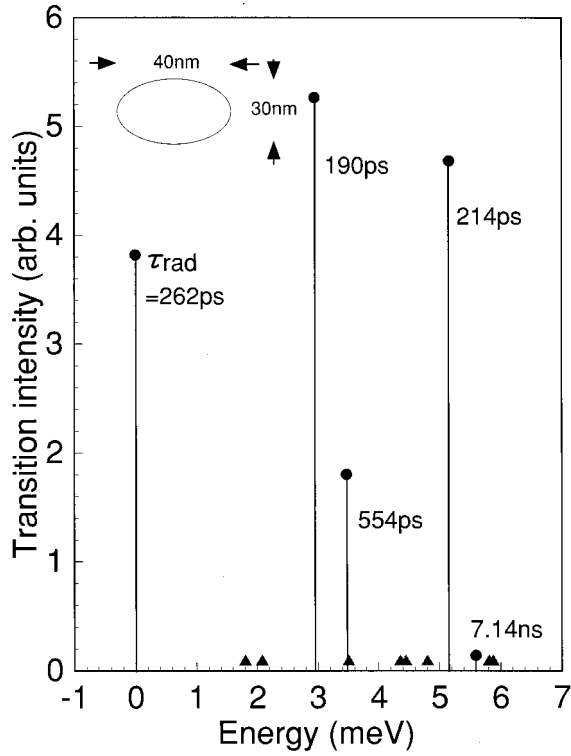


FIG. 4. Exciton energy levels in a GaAs quantum disk with parameters of $a=20$ nm, $b=15$ nm, $L_z=3$ nm, $V_e^0=-6$ meV, and $V_h^0=-3$ meV (see the text). The origin of energy is taken at the exciton ground state. The dark exciton states are denoted by triangles slightly above the horizontal axis.

functional form of the confining potential, and α_x and α_y indicate the degree of the electron-hole correlation and are determined variationally. The electron-hole relative motion within the exciton state is not much different from that in the bulk because the lateral confinement is rather weak. As a result, the parameters α_x and α_y are weakly dependent on the lateral size. Because of the inversion symmetry of the confining potential, the parity is a good quantum number and the wave function can be classified in terms of the combination of parities of $x^{l_e+l_h}$ and $y^{m_e+m_h}$. The exciton ground state belongs to the (even,even) series, where the first (second) index indicates the parity with respect to the x (y) coordinate. As can be seen easily, the optically allowed exciton states belong to the (even,even) series and other exciton states associated with (even,odd), (odd,even), and (odd,odd) series are dark states. In actual calculations, terms up to the sixth power are included, namely, $0 \leq l_e + l_h, m_e + m_h \leq 6$ to ensure the convergence of the calculation.

The potential depth for the exciton lateral motion can be guessed from the splitting energy of the heavy-hole excitons due to the monolayer fluctuation of the QW thickness. The value of $|V_e^0 + V_h^0|$ is typically about 10 meV for the nominal QW thickness about 3 nm.^{9,10} Of course, even if $V_e^0 + V_h^0$ is fixed, each value of V_e^0 and V_h^0 cannot be determined uniquely. Here we employ $V_e^0=-6$ meV and $V_h^0=-3$ meV throughout this paper, referring to the experimental results and assuming $V_e^0:V_h^0=2:1$.

A typical example of the exciton level structure is shown in Fig. 4 for $a=20$ nm and $b=15$ nm. The disk height,

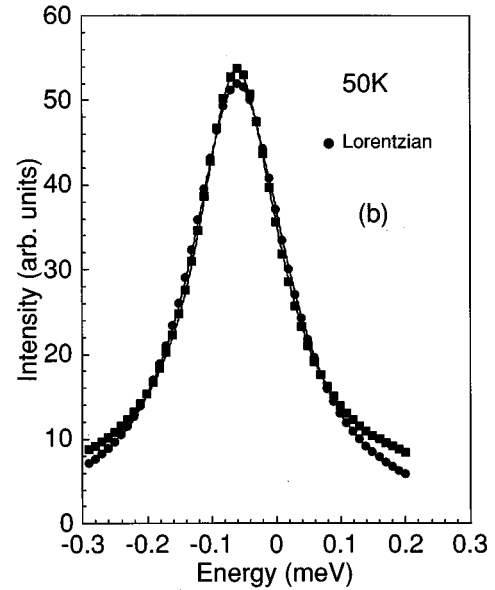
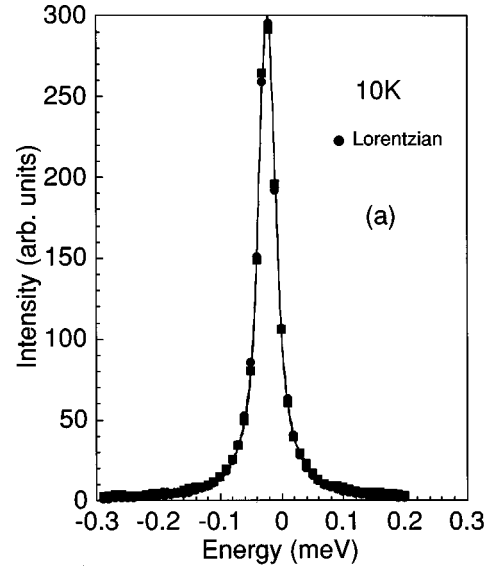


FIG. 5. Absorption spectra of the exciton ground state at (a) 10 K and (b) 50 K for the quantum disk in Fig. 4.

namely, the QW thickness, is fixed at 3 nm throughout this paper. The transition intensities of optically active exciton states are plotted by solid lines and the corresponding radiative lifetime is also given alongside. The dark exciton states are exhibited by triangles slightly above the horizontal axis to indicate the energy positions. In the calculation of the optical-absorption spectrum in Eq. (2.2), the lowest 13 exciton levels are taken into account, including the dark exciton states, because this number of levels is sufficient for converged results.

V. TEMPERATURE DEPENDENCE OF THE EXCITON DEPHASING RATE

First of all, we are interested in the line shape of the calculated absorption spectrum. The line shape of the exciton ground state is plotted in Fig. 5 for a quantum disk model in Sec. IV at 10 and 50 K. The squares show the calculated spectra and the circles are the Lorentzian fit. At low tempera-

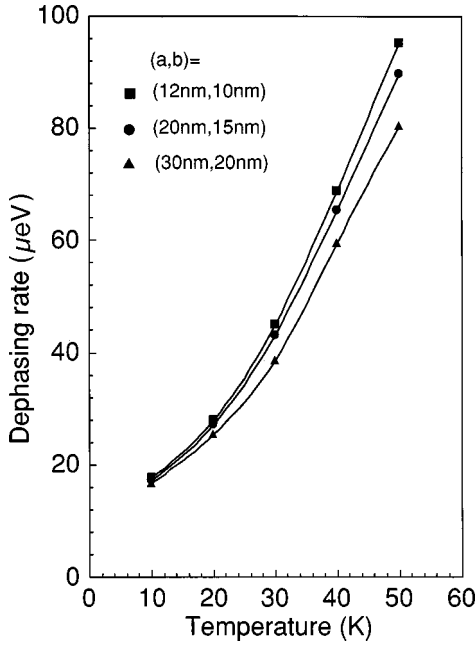


FIG. 6. Dephasing rates are plotted as a function of temperature for the exciton ground state in three quantum disks with size parameters of $(a,b)=(12 \text{ nm}, 10 \text{ nm})$, $(20 \text{ nm}, 15 \text{ nm})$ and $(30 \text{ nm}, 20 \text{ nm})$ and the disk height of 3 nm.

tures, the spectra can be fitted very well by the Lorentzian as expected. At elevated temperatures, however, the line shape deviates from the Lorentzian and shows additional broadening. In any case, the dephasing rate, i.e., the HWHM of the absorption spectrum, can be estimated unambiguously. In addition, it is interesting to note the redshift of the exciton peak position about several tens of μeV relative to the purely electronic transition energy indicated by the origin of energy. This is caused by the lattice relaxation energy given by Eq. (4.5) in Ref. 18.

The size dependence of the dephasing rate is shown in Fig. 6 for the size parameters of $(a,b)=(12 \text{ nm}, 10 \text{ nm})$, $(20 \text{ nm}, 15 \text{ nm})$, and $(30 \text{ nm}, 20 \text{ nm})$. In this size range the dephasing rate is larger for smaller sizes. This can be considered to be caused by the enhanced coupling strength between the exciton and acoustic phonons since the confinement effect on the spectral density of acoustic phonon modes is not significant in this size range. From the comparison of these results with experimental data, we can guess the likely size of the quantum disk. Hereafter we employ the size parameters of $(a,b)=(20 \text{ nm}, 15 \text{ nm})$.

The calculated dephasing rate is plotted in Fig. 7 as a function of temperature with experimental data.¹⁰ As mentioned in the Introduction, the difference between the dephasing rate Γ_{\perp} and half the population decay rate $\Gamma_{\parallel}/2$ indicates the pure dephasing rate. It is seen that the overall agreement between the theory and experiments is satisfactory concerning both the absolute magnitude and the temperature dependence. Furthermore, in theory we can separate out the contribution of the deformation potential coupling to the exciton dephasing and this part is shown by the arrow denoted as ‘‘Def. pot.’’ The remaining part is coming from the piezoelectric coupling and the interference term between the two couplings. This part is simply denoted as ‘‘Piezo.’’ in Fig. 7. It is seen that the deformation potential coupling is

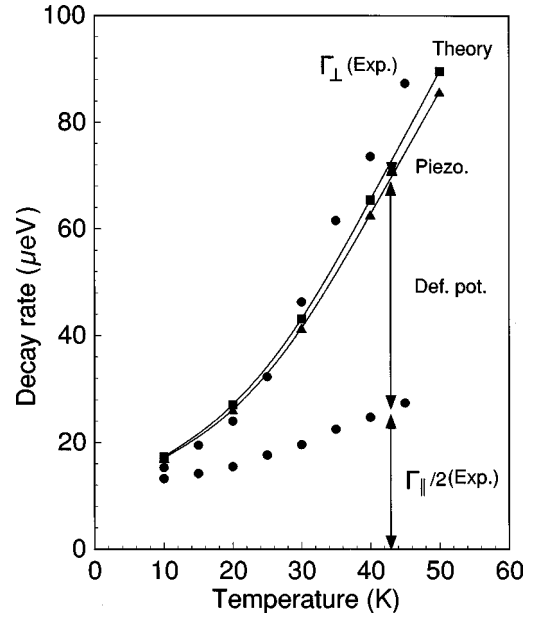


FIG. 7. Calculated dephasing rates of the exciton ground state are shown with experimental data (Ref. 10) as a function of temperature. A quantum disk model is employed with the same parameters as in Fig. 4. The pure dephasing rate is decomposed into the contribution from the deformation potential coupling denoted as ‘‘Def. pot.’’ and that from the piezoelectric coupling and the interference term denoted as ‘‘Piezo.’’

dominantly contributing to the pure dephasing.

In order to see the reason in more detail, we look into the matrix elements of the exciton-phonon interactions. In Fig. 8 we plot the angular average of the squared matrix element of the exciton-phonon interaction defined by

$$f_{ij}^{\alpha}(|q|) = \int d\Omega | \langle i | V_{\alpha}(q) | j \rangle |^2, \quad (5.1)$$

where $\alpha = \text{LA}$ or TA , the indices i and j denote the exciton state, and for the case of $\alpha = \text{TA}$ the contribution from both TA1 and TA2 modes in Eq. (3.3) is combined. V_{LA} includes the contribution from both the deformation potential coupling and the piezoelectric coupling, whereas V_{TA} contains only the contribution from the piezoelectric coupling. In the inset, the energy-level scheme is shown for the lowest four exciton states, including the dark exciton states. From the comparison between Figs. 8(a) and 8(b), we see that the contribution from LA phonons is more than one order of magnitude larger than that from TA phonons. Furthermore, it is important to note that the wave vector of the most efficiently coupled phonons is roughly determined by $\max(1/a_B, 1/L)$, where a_B is the exciton Bohr radius and L is the typical size of the lateral confinement. The vanishing z component of the wave vector is favored because the common envelope function in Eq. (4.3) is assumed for both the electron and the hole and they are uncorrelated in the z direction. The relevant wave vector is about 10^6 cm^{-1} for GaAs islands. Hence the corresponding phonon energy is rather small ($< 1 \text{ meV}$), since the phonon energy versus wave-vector ($|q|$) relation is $\hbar\omega = 0.32(0.22)|q|$ (meV) for the LA (TA) modes with $|q|$ scaled in units of 10^6 cm^{-1} . This property will be invoked

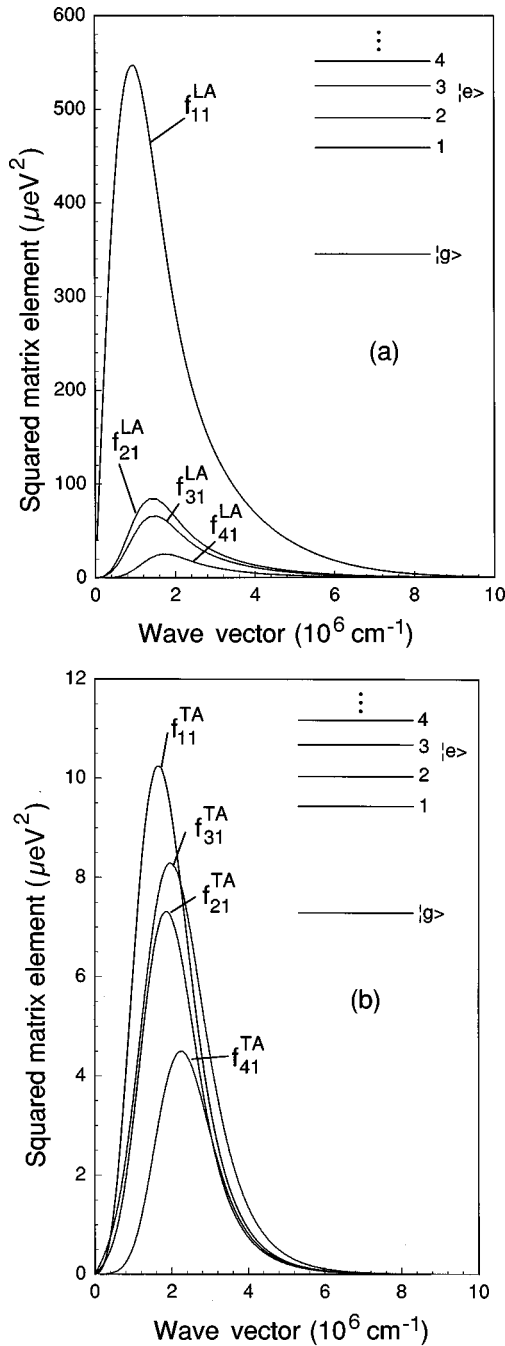


FIG. 8. Angularly averaged squared matrix elements of the exciton-phonon interaction are plotted as a function of the phonon wave vector for (a) the LA phonons and (b) the TA phonons. The horizontal (vertical) axis is scaled by 10^6 cm^{-1} [$(\mu\text{eV})^2$]. The employed GaAs quantum disk is the same as in Fig. 4. The lowest four exciton states are numbered consecutively including the dark exciton states.

later in discussing the correlation between the temperature dependence of the exciton dephasing rate and the strength of the quantum confinement.

We have also calculated the dephasing rate of the excited exciton states. The results are shown in Fig. 9 for the lowest four optically active exciton states. In the calculation for the excited exciton states, the value of δ in Eq. (2.19) is assumed to be the same as for the exciton ground state because the relevant relaxation processes mentioned above Eq. (2.19)

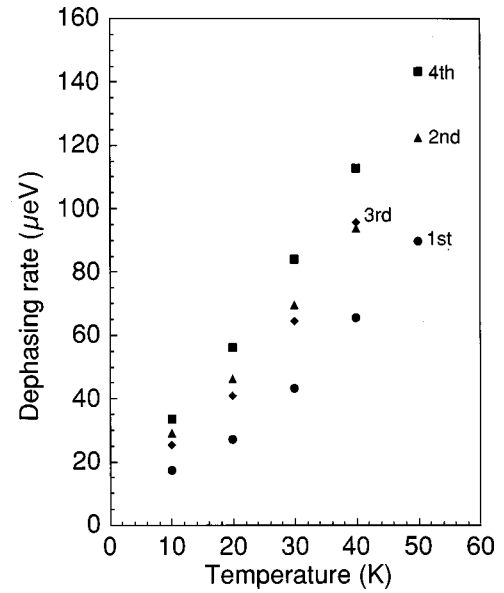


FIG. 9. Calculated dephasing rates of the lowest four optically active exciton states are shown as a function of temperature for the same quantum disk as in Fig. 4.

may be dependent on the exciton state but the absolute magnitude of δ is rather small. The dephasing rate is in general larger for the higher-lying exciton states. But this tendency is not monotonic as seen by the reversed order of magnitude between the second and third exciton states.

VI. ELEMENTARY PROCESSES OF EXCITON PURE DEPHASING

Now we discuss the mechanism of exciton pure dephasing. Generally speaking, pure dephasing means the decay of the dipole coherence without change in the state of the system. Any real transition to other states leads to the population decay. Thus the pure dephasing is caused by virtual processes which start from a relevant state and through some excursion in the intermediate states return to the same initial state. These virtual processes give rise to the temporal fluctuation of the phase of wave function. Previously this kind of temporal phase fluctuation was treated by a stochastic model of random frequency modulation²¹ and the resulting pure dephasing was discussed in the context of resonant secondary emission.²²

Here we treat these processes microscopically. There are two kinds of such virtual processes which contribute to the pure dephasing. The first kind of process is induced by the off-diagonal exciton-phonon interaction. These processes start from the exciton ground state, pass through excited exciton states, and return to the exciton ground state. The second kind of process is induced by the diagonal exciton-phonon interaction and the relevant state remains always within the exciton ground state. These processes are shown schematically in the inset of Fig. 10. The contribution to the pure dephasing from the second kind of process can be singled out theoretically by carrying out the calculation which includes only the exciton ground state. That contribution is denoted by ‘‘Intra-exciton ground state’’ in Fig. 10. The remaining part, denoted as ‘‘Excited exciton states,’’

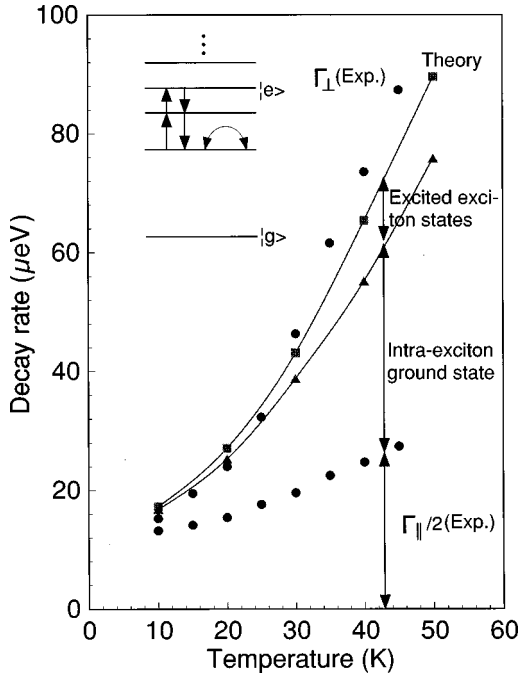


FIG. 10. Calculated dephasing rates of the exciton ground state are shown with experimental data (Ref. 10) as a function of temperature for the same quantum disk as in Fig. 4. The pure dephasing rate is decomposed into the contribution from the diagonal exciton-phonon interaction denoted as “Intra-exciton ground state” and that from the off-diagonal interaction and the interference term denoted as “Excited exciton states.”

comes from the first kind of process and the interference between the two kinds of processes. It is seen that the intra-exciton ground state (diagonal) process contributes substantially to the pure dephasing but the contribution from the off-diagonal process is not negligible. This feature can be understood from Figs. 8(a) and 8(b) since the squared matrix element within the exciton ground state, denoted by f_{11}^{α} , is much larger than other squared matrix elements. As a result, the intra-exciton ground state process contributes significantly to the pure dephasing.

VII. MECHANISMS OF POPULATION DECAY OF EXCITONS

The possible mechanisms of the population decay will be discussed. Experimentally, two decay time constants were observed.¹⁰ The slow time constant (~ 200 ps) is almost independent of temperature, suggesting the radiative decay as its mechanism. In fact, the calculated radiative lifetime of the exciton ground state is around 200 ps as shown in Fig. 4. On the other hand, the fast time constant (~ 30 ps) is weakly dependent on temperature. The likely mechanisms are the thermal activation to excited exciton states and the phonon-assisted migration to neighboring islands. In this section we present a detailed calculation of these relaxation rates and examine the significance of these mechanisms.

A. Phonon-assisted population relaxation

The phonon-assisted transition rate to other exciton states is calculated as

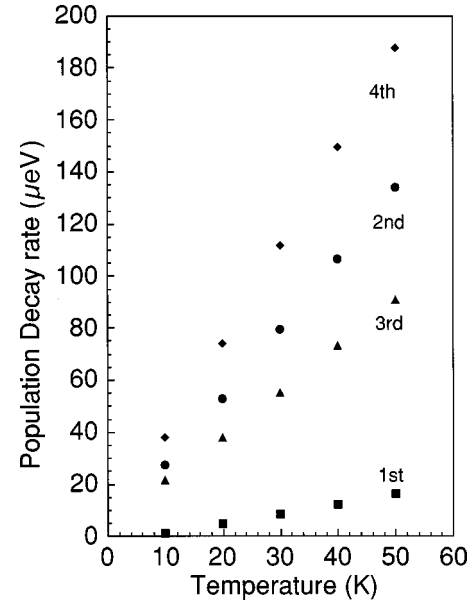


FIG. 11. Phonon-assisted population decay rates of the lowest four optically active exciton states are plotted as a function of temperature for the same quantum disk as in Fig. 4.

$$P_i = \sum_{j \neq i} w_{ij}, \quad (7.1)$$

where w_{ij} is the transition rate from the exciton state i to the other exciton state j . Here P_i 's are calculated for the lowest four optically active exciton states and are plotted in Fig. 11 as a function of temperature. The same quantum disk model as in Fig. 4 is employed and the same 13 exciton levels are included in the calculation. Since the energy difference between exciton levels is less than several meV, it is sufficient to take into account only the one-phonon processes. For the exciton ground state, the transition rate is about several μeV . For the excited exciton states, the transition rates are about one order of magnitude larger than that of the exciton ground state. In general, the higher-lying exciton states have a larger population decay rate. But this trend is not monotonic as seen by the reversed order of magnitude between the second and third exciton states.

It is interesting to note that the linear temperature dependence is clearly seen. This indicates that the energy of the relevant acoustic phonons is rather small as shown in Figs. 8(a) and 8(b) and the high-temperature approximation holds as

$$\frac{1}{e^{\hbar\omega/k_B T} - 1} \approx \frac{k_B T}{\hbar\omega}. \quad (7.2)$$

This is the origin of the linear temperature dependence.

B. Phonon-assisted exciton migration

The excitons localized at island structures can migrate among them accompanying phonon absorption or emission to compensate for the energy mismatch. Since the energy mismatch is typically about a few meV, the acoustic phonons are dominantly contributing to the exciton migration process. Now let us consider two island sites at R_a and R_b and as-

sume that the island at R_b is larger in size and has a localized exciton state of lower energy than in the island at R_a . Then we consider the phonon-assisted exciton migration from the site R_a to the site R_b , namely, a transition of

$$|R_a; n_q\rangle \rightarrow |R_b; n_q + 1\rangle,$$

where n_q indicates the occupation number of an acoustic-phonon mode with wave vector \vec{q} . As discussed previously,²³ there are three elementary processes of this transition,

$$(i) |R_a; n_q\rangle \xrightarrow{H_{ep}} |R_b; n_q + 1\rangle,$$

$$(ii) |R_a; n_q\rangle \xrightarrow{H_{ep}} |R_a; n_q + 1\rangle \xrightarrow{H_{ss}} |R_b; n_q + 1\rangle,$$

$$(iii) |R_a; n_q\rangle \xrightarrow{H_{ss}} |R_b; n_q\rangle \xrightarrow{H_{ep}} |R_b; n_q + 1\rangle,$$

where H_{ep} (H_{ss}) represents the exciton-phonon interaction (intersite transfer) Hamiltonian. The first process is a direct process through the overlap between exciton wave functions at two island sites which is strongly dependent on the distance between two islands. Thus this process contributes only for the case of a short distance. On the other hand, the second and third processes are indirect ones which can contribute to the exciton transfer even for the case of long distance.

The intersite transfer Hamiltonian H_{ss} is caused by the electron-electron interaction and is calculated as

$$\begin{aligned} J(R_a, R_b) &= \langle R_a | H_{ss} | R_b \rangle \\ &= \sum_{r'_e, r'_h} \sum_{r_e, r_h} F_{c\tau, v\sigma}^*(r_e, r_h; R_a) F_{c\tau', v\sigma'}(r'_e, r'_h; R_b) \\ &\quad \times [V(c\tau r_e, v\sigma' r'_h; c\tau' r'_e, v\sigma r_h) \\ &\quad - V(c\tau r_e, v\sigma' r'_h; v\sigma r_h, c\tau' r'_e)], \end{aligned} \quad (7.3)$$

where the localized exciton at the site R_i is described as

$$|R_i\rangle = \sum_{\tau, r_e; \sigma, r_h} F_{c\tau, v\sigma}(r_e, r_h; R_i) a_{c\tau r_e}^\dagger a_{v\sigma r_h} |0\rangle \quad (7.4)$$

with an envelope function F corresponding to Eq. (4.2), and the suffix τ (σ) denotes the Wannier function index of the conduction (valence) band, e.g., the total angular momentum. The first term in Eq. (7.3) represents the electron-hole exchange interaction and the second term corresponds to the Coulomb interaction. Because of the localized nature of the Wannier functions, we can approximate as

$$\begin{aligned} V(c\tau r_e, v\sigma' r'_h; v\sigma r_h, c\tau' r'_e) &\approx \delta_{r'_e r_e} \delta_{r'_h r_h} \delta_{\tau\tau'} \delta_{\sigma\sigma'} \frac{e^2}{\epsilon |r_e - r_h|}, \\ V(c\tau r_e, v\sigma' r'_h; c\tau' r'_e, v\sigma r_h) &\approx \delta_{r_e r_h} \delta_{r'_e r'_h} \left[\delta_{r'_e r_e} V(c\tau r_e, v\sigma' r_e; c\tau' r_e, v\sigma r_e) \right. \\ &\quad \left. + (1 - \delta_{r_e r'_e}) \frac{\vec{\mu}_{c\tau v\sigma} [1 - 3\vec{n} \cdot \vec{n}]}{|r_e - r'_e|^3} \vec{\mu}_{v\sigma' c\tau'} \right], \end{aligned} \quad (7.5)$$

with

$$\vec{n} = \frac{\vec{r}_e - \vec{r}'_e}{|r_e - r'_e|}, \quad (7.6)$$

$$\vec{\mu}_{c\tau v\sigma} = \int d^3r \phi_{c\tau R}^*(r) (\vec{r} - \vec{R}) \phi_{v\sigma R}(r), \quad (7.7)$$

where $\phi_{c\tau(v\sigma)R}(r)$ is a Wannier function localized at the site R . Hereafter the vector symbols will be dropped because there is no fear of confusion. The Coulomb term decreases rapidly when $|R_a - R_b|$ exceeds the lateral size of the exciton wave function. On the other hand, the exchange term contains the dipole-dipole interaction and has a long-range character decreasing as $|R_a - R_b|^{-3}$. Thus the exchange term contributes dominantly to the intersite exciton transfer when $|R_a - R_b|$ is larger than the lateral size of the confining potential.

The exciton transfer probability is calculated as

$$\begin{aligned} w(R_a \rightarrow R_b) &= \frac{2\pi}{\hbar} \sum_{\sigma} \left| \langle R_b; n_q + 1 | H_{ep}^{\sigma} | R_a; n_q \rangle + \frac{\langle R_b; n_q + 1 | H_{ss} | R_a; n_q + 1 \rangle \langle R_a; n_q + 1 | H_{ep}^{\sigma} | R_a; n_q \rangle}{-\hbar \omega_q^{\sigma}} \right. \\ &\quad \left. + \frac{\langle R_b; n_q + 1 | H_{ep}^{\sigma} | R_b; n_q \rangle \langle R_b; n_q | H_{ss} | R_a; n_q \rangle}{E_X(R_a) - E_X(R_b)} \right|^2 \delta(E_X(R_a) - E_X(R_b) - \hbar \omega_q^{\sigma}), \end{aligned} \quad (7.8)$$

where $E_X(R_i)$ is the energy of a localized exciton at the site R_i and the summation concerning the acoustic-phonon mode σ is taken over the LA, TA1, and TA2 modes in Eq. (3.3).

In the exchange matrix element in Eq. (7.5), the first (second) term is usually called the short- (long-) range part of the exchange interaction. The contribution from the long-range part can be rewritten into a more tractable form as²⁴

$$\begin{aligned}
& \sum_{r_e \neq r'_e} F_{c\tau, v\sigma}^*(r_e, r_e; R_a) F_{c\tau', v\sigma'}(r'_e, r'_e; R_b) \mu_{c\tau, v\sigma} \frac{[1 - 3n \cdot \hat{n}]}{|r_e - r'_e|^3} \mu_{v\sigma', c\tau'} \\
&= - \sum_{r_e \neq r'_e} F_{c\tau, v\sigma}^*(r_e, r_e; R_a) \mu_{c\tau, v\sigma} \text{grad}_{r_e} \text{div}_{r'_e} \left[\frac{\mu_{v\sigma', c\tau'}}{|r_e - r'_e|} F_{c\tau', v\sigma'}(r'_e, r'_e; R_b) \right] \\
&= - \int d^3 r_e \int' d^3 r'_e F_{c\tau, v\sigma}^*(r_e, r_e; R_a) \mu_{c\tau, v\sigma} \text{grad}_{r_e} \text{div}_{r'_e} \left[\frac{\mu_{v\sigma', c\tau'}}{|r_e - r'_e|} F_{c\tau', v\sigma'}(r'_e, r'_e; R_b) \right], \tag{7.9}
\end{aligned}$$

where the integration with respect to r'_e is carried out over the whole space, excluding a small sphere around the point r_e , and this is indicated by a primed integral symbol. Then making use of a relation for an arbitrary vector field $\vec{Q}(r)$,

$$\int' d^3 r' \text{grad}_{r'} \text{div}_{r'} \frac{\vec{Q}(r')}{|r - r'|} = \frac{4\pi}{3} \vec{Q}(r) + \text{grad}_{r'} \text{div}_{r'} \int' d^3 r' \frac{\vec{Q}(r')}{|r - r'|}, \tag{7.10}$$

we can rewrite Eq. (7.9) as

$$- \int d^3 r_e F_{c\tau, v\sigma}^*(r_e, r_e; R_a) \mu_{c\tau, v\sigma} \left[\frac{4\pi}{3} \mu_{v\sigma', c\tau'} F_{c\tau', v\sigma'}(r_e, r_e; R_b) + \text{grad}_{r_e} \text{div}_{r_e} \int d^3 r'_e \frac{\mu_{v\sigma', c\tau'}}{|r_e - r'_e|} F_{c\tau', v\sigma'}(r'_e, r'_e; R_b) \right], \tag{7.11}$$

where in the second term within the parentheses the integration can be performed over the whole space because the singularity of $|r_e - r'_e|^{-1}$ is integrable. By a partial integration, we have the expression of the long-range exchange term as

$$\begin{aligned}
& - \frac{4\pi}{3} (\mu_{c\tau, v\sigma} \cdot \mu_{v\sigma', c\tau'}) \int d^3 r F_{c\tau, v\sigma}^*(r, r; R_a) F_{c\tau', v\sigma'}(r, r; R_b) \\
& + \int d^3 r \text{div}_r [F_{c\tau, v\sigma}^*(r, r; R_a) \mu_{c\tau, v\sigma}] \text{div}_r \left[\int d^3 r' \frac{\mu_{v\sigma', c\tau'}}{|r - r'|} F_{c\tau', v\sigma'}(r', r'; R_b) \right]. \tag{7.12}
\end{aligned}$$

The short-range exchange term is simply written as

$$\begin{aligned}
& V(c\tau r_0, v\sigma' r_0; c\tau' r_0, v\sigma r_0) \\
& \times \int d^3 r F_{c\tau, v\sigma}^*(r, r; R_a) F_{c\tau', v\sigma'}(r, r; R_b) \tag{7.13}
\end{aligned}$$

and the Coulomb term is calculated by

$$\begin{aligned}
& - \int d^3 r_e \int d^3 r_h F_{c\tau, v\sigma}^*(r_e, r_h; R_a) \frac{e^2}{\epsilon |r_e - r_h|} \\
& \times F_{c\tau, v\sigma}(r_e, r_h; R_b). \tag{7.14}
\end{aligned}$$

Combining three terms (7.12), (7.13), and (7.14), we can estimate the exciton transfer matrix element in Eq. (7.3).

It is to be noted that when the Coulomb term and/or the exchange term are of comparable magnitude to the energy difference between localized exciton states at R_a and R_b , the eigenstates should be mixed states of two localized excitons and a simple picture of exciton transfer between two sites cannot be applied. Thus we have to check the inequality

$$|J(R_a, R_b)| \ll |E_X(R_a) - E_X(R_b)|$$

before we apply the exciton transfer model. We can check numerically that the matrix element $|J(R_a, R_b)|$ is typically about several tens of μeV except for a very close pair of islands, whereas $|E_X(R_a) - E_X(R_b)|$ is about a few meV for

typical sizes of islands. Thus the simple picture of exciton transfer can be applied safely.

In order to see the typical behavior of the exciton migration rate, we employ two quantum disk islands characterized by $L_z = 3$ nm and the lateral size parameters of $(a, b) = (20 \text{ nm}, 15 \text{ nm})$ and $(30 \text{ nm}, 20 \text{ nm})$ and consider the migration between two exciton ground states whose energy difference is 0.68 meV. The exciton migration rate depends on the distance between two islands, the geometrical configuration of two islands, and on the direction of exciton polarizations. In Figs. 12(a) and 12(b), the migration rate is plotted as a function of the center-to-center distance between two islands. In Fig. 12(a), two islands are aligned such that the longer axes of two ellipses are coincident with each other. In this configuration, the migration rate is larger for the exciton polarization along the longer axis than for the exciton polarization along the shorter axis because of the larger interaction through the surface charges. In Fig. 12(b), two islands are aligned such that the shorter axes of two ellipses are coincident with each other. In this configuration, the migration rate is larger for the exciton polarization along the shorter axis than for the exciton polarization along the longer axis. The absolute magnitude of the exciton migration rate is about several tens of μeV .

We have also estimated the migration rate between the exciton ground state and the excited exciton states. The results are shown in Fig. 13 for the transition from the exciton

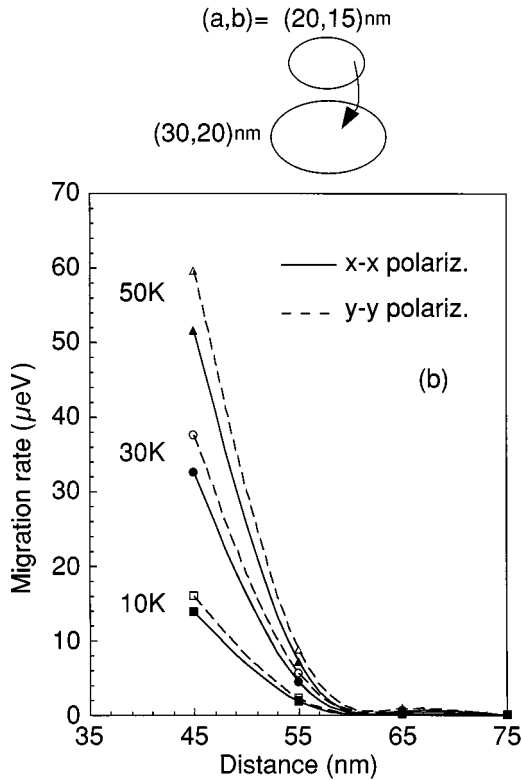
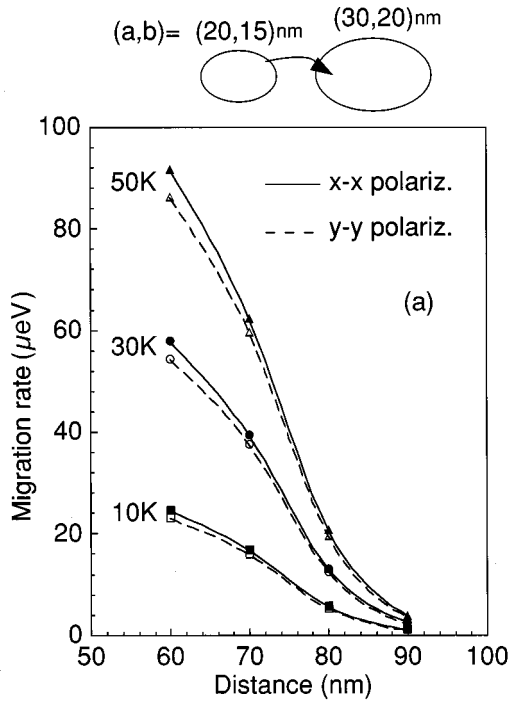


FIG. 12. Phonon-assisted migration rate from the exciton ground state in a quantum disk of $(a,b)=(20 \text{ nm}, 15 \text{ nm})$ to the exciton ground state in a quantum disk of $(a,b)=(30 \text{ nm}, 20 \text{ nm})$ is plotted as a function of the center-to-center distance between two quantum disks at temperatures of 10, 30, and 50 K. In (a) [(b)], two disks are aligned such that the longer (shorter) axes of the two ellipses are coincident with each other and the distance is measured along the longer (shorter) axis. The exciton polarization in two disks is aligned along the x or y direction and this is indicated by $x-x$ or $y-y$ polariz., where $x(y)$ denotes the direction of the longer (shorter) axis of the ellipse.

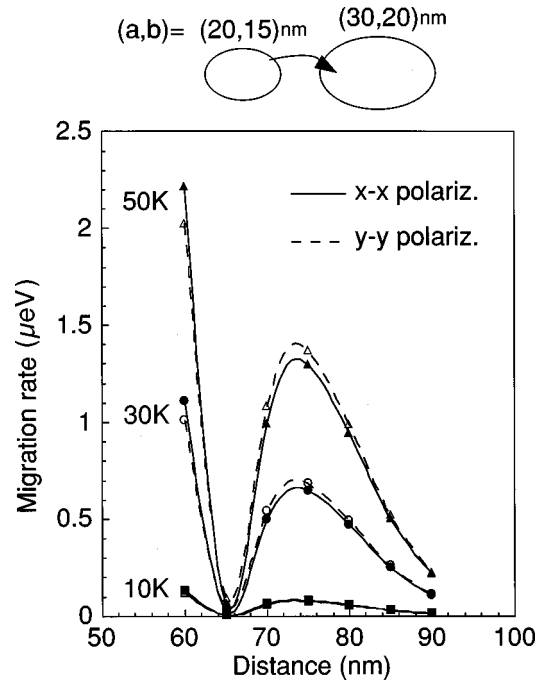


FIG. 13. Phonon-assisted migration rate from the exciton ground state in a quantum disk of $(a,b)=(20 \text{ nm}, 15 \text{ nm})$ to the second lowest optically active exciton state in a quantum disk of $(a,b)=(30 \text{ nm}, 20 \text{ nm})$ is plotted as a function of the center-to-center distance between two quantum disks at temperatures of 10, 30, and 50 K. The configuration of two disks is the same as in Fig. 12(a).

ground state of an island with $(a,b)=(20 \text{ nm}, 15 \text{ nm})$ to the second optically active exciton state in an island with $(a,b)=(30 \text{ nm}, 20 \text{ nm})$. The configuration of two islands is the same as in Fig. 12(a). This migration process is associated with phonon absorption ($\sim 2.11 \text{ meV}$) in contrast to the case in Fig. 12. As a result, the migration rate is several tens times smaller than in Fig. 12(a). In addition, the distance dependence is not monotonic. This feature arises from the interference among three terms in Eq. (7.8) and may be sensitively dependent on the spatial profile of the exciton wave function.

At present, the distance between neighboring islands cannot be determined precisely. But from the consideration on the order of magnitude, we can identify the likely mechanism of the population decay of the exciton ground state as the combination of thermal activation to the excited exciton states within an island and phonon-assisted exciton migration to neighboring islands.

VIII. CORRELATION BETWEEN TEMPERATURE DEPENDENCE OF EXCITON DEPHASING RATE AND STRENGTH OF QUANTUM CONFINEMENT

We have so far discussed the dephasing rate of excitons in GaAs QD-like islands. It is important to note that the temperature dependence of exciton dephasing rates can differ qualitatively for semiconductors with strong and weak quantum confinement. For quantum dots belonging to the strong confinement regime, such as II-VI nanocrystals, a linear temperature dependence was observed up to 200 K.¹⁴ Recent

more careful measurements show also the linear temperature dependence, although the measured temperature range is limited below 30 K.²⁵ On the other hand, for CuCl nanocrystals belonging to the weak confinement regime since the exciton Bohr radius is rather small, a temperature dependence similar to that in Fig. 7 was observed,^{15,26} although strongly nonlinear temperature dependence occurs above a higher temperature than in Fig. 7. These different temperature dependencies can be explained by the present theory if we take into account the different exciton level structures involved. For GaAs islands with lateral size about 40 nm the energy separation among the lowest exciton levels is about a few meV, and for CuCl nanocrystals with 4-nm radius the energy separation is typically several meV. On the other hand, in CdSe nanocrystals with radii smaller than 2 nm, the relevant energy spacing is determined by the *A*- and *B*-exciton splitting (~ 26 meV) instead of the intersublevel energy of the *A*-exciton series which is much larger.²⁷

The key feature in considering the temperature dependence of the exciton dephasing is the interplay among virtual processes within the exciton ground state, those which pass through excited exciton states and real transitions to excited exciton states. Another important feature is the phonon-mode spectra. In this paper, we have been dealing with the continuous spectra of acoustic phonons which is justified because of the small difference in the elastic properties between the QW material and the barrier material. The situation is slightly different in the case of CuCl and CdSe nanocrystals. They are embedded in materials with much different elastic properties. Here the acoustic phonons are affected by the elastic confinement^{28,29} but are intrinsically delocalized into the surrounding medium. As a result, the mode spectra of acoustic phonons have a continuous background in addition to discrete peaks corresponding to size-quantized modes.³⁰ Furthermore, as discussed in Sec. V, it is important to note that the wave vector of phonons which couple most strongly with excitons is roughly given by $\max(1/a_B, 1/L)$, where L is the typical size of nanocrystals.

In the case of small CdSe nanocrystals, the energy separation between the exciton ground state and the first excited exciton state is about 20 meV and the acoustic-phonon energy corresponding to the maximum coupling with excitons is about 1 meV. Thus only the virtual processes within the exciton ground state contribute to the exciton dephasing up to around 200 K. Then the high-temperature approximation in Eq. (7.2) holds, leading to the linear temperature dependence of the dephasing rate. Above 200 K, the multi-acoustic-phonon and LO-phonon assisted activation to the excited exciton states becomes possible, yielding the nonlinear temperature dependence of the dephasing rate.

In the case of GaAs islands, the energy of phonons which couple strongly with excitons is less than 1 meV. Thus at low temperatures (≤ 10 K), the virtual processes within the exciton ground state contribute dominantly to the exciton dephasing. At elevated temperatures (~ 30 K), the virtual processes via excited exciton states begin to contribute to the exciton dephasing, because the energy separation between the ground and first excited exciton states is a few meV. Thus the range of the linear temperature dependence is rather narrow and the nonlinear temperature dependence prevails.

In the case of CuCl nanocrystals, the phonon energy cor-

responding to the maximum coupling with excitons is estimated as about 3–4 meV. Also the energy separation among exciton levels is several meV. Thus the linear temperature dependence is not manifest and the nonlinear temperature dependence becomes prominent above 50 K.

Thus we see that the temperature dependence of the exciton dephasing rate is sensitively dependent on the exciton level structures, which reflect the strength of quantum confinement, and on the energy of phonons, which couple strongly with excitons. We can summarize as follows. In the strong confinement regime, the diagonal virtual processes dominate the pure dephasing in which the relevant state remains always within the exciton ground state and the electron-phonon interactions associated with small energy acoustic phonons are mainly contributing to the pure dephasing. Thus the high-temperature approximation holds for the phonon occupation number, leading to the linear temperature dependence of the dephasing rate up to the temperature corresponding to the energy spacing between the ground and first excited exciton states. On the other hand, in the weak confinement regime, the exciton levels are rather densely distributed and the off-diagonal virtual processes contribute substantially to the pure dephasing in which the virtual transition to excited exciton states occurs effectively when the thermal energy $k_B T$ approaches the relevant energy-level separation. In this case, acoustic phonons having the thermal energy contribute significantly to the exciton dephasing. As a result, the linear temperature dependence is not manifest and the nonlinear temperature dependence appears dominantly.

IX. SUMMARY AND DISCUSSION

We have formulated a theory of exciton dephasing in semiconductor quantum dots extending the Huang-Rhys theory of *F* centers to include the mixing among the exciton state manifold through the exciton-phonon interaction and we identified the mechanisms of pure dephasing. We have reproduced quantitatively the magnitude as well as the temperature dependence of the exciton dephasing rate observed in GaAs QD-like islands. In this system, it has been found that both the diagonal and off-diagonal exciton-phonon interactions are contributing to the exciton pure dephasing on the same order of magnitude. Examining the previous data of the exciton dephasing rate in GaAs islands, CuCl and CdSe nanocrystals, we have pointed out the correlation between the temperature dependence of the dephasing rate and the strength of the quantum confinement and explained gross features of the temperature dependence in various materials quantum dots. Furthermore, we have discussed likely mechanisms of the exciton population decay.

Very recently, a detailed study of the exciton dephasing rate in CuCl nanocrystals was carried out down to much lower temperatures and an unusual temperature dependence was reported.³¹ A two-level system (TLS) with a very small energy splitting was proposed as a possible mechanism of this unusual temperature dependence. At very low temperatures, the acoustic phonons are frozen out and the only remaining degrees of freedom may be a TLS which acts as an agent of the exciton dephasing.³² The two-level system is considered as some local modification of atomic configura-

tion but more details are yet to be clarified. At further lower temperatures, all the degrees of freedom are frozen out and the exciton dephasing is mainly caused by the radiative decay, approaching the limiting situation that $1/T_2 = 1/(2T_1)$.

ACKNOWLEDGMENT

The author would like to thank Professor Hailin Wang for the close collaboration and illuminating discussions.

-
- ¹See, for example, *Confined Electrons and Photons, New Physics and Devices*, edited by E. Burstein and C. Weisbuch (Plenum, New York, 1995); *Microcrystalline and Nanocrystalline Semiconductors*, edited by R. W. Collins, C. C. Tsai, M. Hirose, F. Koch, and L. Brus, Materials Research Society Symposium Proceedings No. 358 (Materials Research Society, Pittsburgh, 1995).
- ²J. Hegarty and M. D. Sturge, *J. Opt. Soc. Am. B* **2**, 1143 (1985).
- ³M. D. Webb, S. T. Cundiff, and D. G. Steel, *Phys. Rev. B* **43**, 12 658 (1991).
- ⁴L. Schultheis, A. Honold, J. Kuhl, K. Köhler, and C. W. Tu, *Phys. Rev. B* **34**, 9027 (1986).
- ⁵A. Honold, L. Schultheis, J. Kuhl, and C. W. Tu, *J. Opt. Soc. Am. B* **4**, S210 (1987).
- ⁶T. Takagahara, *Phys. Rev. B* **32**, 7013 (1985); *J. Lumin.* **44**, 347 (1989).
- ⁷H. F. Hess, E. Betzig, T. D. Harris, L. N. Pfeiffer, and K. W. West, *Science* **264**, 1740 (1994).
- ⁸K. Brunner, G. Abstreiter, G. Böhm, G. Tränkle, and G. Weimann, *Phys. Rev. Lett.* **73**, 1138 (1994).
- ⁹D. Gammon, E. S. Snow, B. V. Shanabrook, D. S. Katzer, and D. Park, *Science* **273**, 87 (1996); *Phys. Rev. Lett.* **76**, 3005 (1996).
- ¹⁰Xudong Fan, T. Takagahara, J. E. Cunningham, and Hailin Wang, *Solid State Commun.* **108**, 857 (1998).
- ¹¹K. Huang and A. Rhys, *Proc. R. Soc. London, Ser. A* **204**, 406 (1950).
- ¹²C. B. Duke and G. D. Mahan, *Phys. Rev.* **139**, A1965 (1965).
- ¹³R. Kubo and Y. Toyozawa, *Prog. Theor. Phys.* **13**, 160 (1955).
- ¹⁴R. W. Schoenlein, D. M. Mittleman, J. J. Shiang, A. P. Alivisatos, and C. V. Shank, *Phys. Rev. Lett.* **70**, 1014 (1993).
- ¹⁵T. Itoh and M. Furumiya, *J. Lumin.* **48&49**, 704 (1991).
- ¹⁶H. Benisty, C. M. Sotomayor-Torres, and C. Weisbuch, *Phys. Rev. B* **44**, 10 945 (1991).
- ¹⁷U. Bockelmann, *Phys. Rev. B* **48**, 17 637 (1993).
- ¹⁸T. Takagahara, *Phys. Rev. Lett.* **71**, 3577 (1993); *J. Lumin.* **70**, 129 (1996) and references therein.
- ¹⁹A. Blacha, H. Presting, and M. Cardona, *Phys. Status Solidi B* **126**, 11 (1984).
- ²⁰*Physics of Group IV Elements and III-V Compounds*, edited by O. Madelung, M. Schulz, and H. Weiss, Landolt-Börnstein, New Series, Group III, Vol. 17, Pt. a (Springer, Berlin, 1982).
- ²¹R. Kubo, in *Fluctuation, Relaxation and Resonance in Magnetic Systems*, edited by D. ter Haar (Oliver and Boyd, Edinburgh, 1962), p. 23.
- ²²T. Takagahara, E. Hanamura, and R. Kubo, *J. Phys. Soc. Jpn.* **43**, 802 (1977); **43**, 811 (1977); **43**, 1522 (1977).
- ²³T. Takagahara, *Phys. Rev. B* **31**, 6552 (1985).
- ²⁴T. Takagahara, *Phys. Rev. B* **47**, 4569 (1993).
- ²⁵Y. Masumoto, K. Takemoto, T. Shoji, and B. R. Hyun, in *Proceedings of the 24th International Conference on the Physics of Semiconductors, Jerusalem, 1998* (World Scientific, Singapore, 1999).
- ²⁶K. Inoue, R. Kuribayashi, K. Sakoda, and A. V. Baranov, *OSA Tech. Dig. Ser. (CLEO'98)* **6**, 266 (1998).
- ²⁷Al. L. Efros, M. Rosen, M. Kuno, M. Nirmal, D. J. Norris, and M. Bawendi, *Phys. Rev. B* **54**, 4843 (1996); detailed calculation was done here including the electron-hole exchange interaction and the effect of nonspherical shape. The typical energy splitting is about 20 meV for a 20-Å radius spherical CdSe quantum dot.
- ²⁸A. E. H. Love, *A Treatise on the Mathematical Theory of Elasticity* (Dover, New York, 1944).
- ²⁹A. Tamura, K. Higeta, and T. Ichinokawa, *J. Phys. C* **15**, 4975 (1982).
- ³⁰A. I. Ekimov (private communication); A. V. Fedorov (private communication).
- ³¹M. Ikezawa and Y. Masumoto, in *Proceedings of the 24th International Conference on the Physics of Semiconductors* (Ref. 25).
- ³²See, for example, *Dynamical Processes in Disordered Systems*, edited by W. M. Yen, Materials Science Forum Vol. 50 (Trans Tech Publications, Switzerland, 1989); *Optical Spectroscopy of Glasses*, edited by I. Zschokke (Reidel Publishing Company, Dordrecht, 1986).